

Article

Preparation of Co-CNK-OH and Its Performance in Fenton-like Photocatalytic Degradation of Tetracycline

Dongrui Hou¹, Jing Luo², Qinggong Sun², Mengyang Zhang¹ and Jianfeng Wang^{1,*}

¹ School of Ecology and Environment, Zhengzhou University, Zhengzhou 450000, China; 202022392015719@gs.zzu.edu.cn (D.H.); 202022392015766@gs.zzu.edu.cn (M.Z.)

² School of Chemical Engineering, Zhengzhou University, Zhengzhou 450000, China; 202022232014616@gs.zzu.edu.cn (J.L.); 202022232014627@gs.zzu.edu.cn (Q.S.)

* Correspondence: wangjf@zzu.edu.cn

Abstract: In this study, Co-modified alkalized g-C₃N₄ (named Co-CNK-OH) was prepared for the Fenton-like photocatalytic degradation of tetracycline (TC) via a simple yet effective calcination-impregnation method. In all samples of CNK-OH with different Co²⁺ loadings, Co-CNK-OH catalyst with the optimal content (9%) exhibited the highest catalytic activity, with 87.1% tetracycline removal and 50% removal efficiency of the total organic carbon (TOC). Mechanism studies revealed that the 9%Co-CNK-OH catalyst had the lower electrical resistance after alkalization treatment and Co²⁺ modification, leading to a significantly accelerated interfacial charge transfer to the electron acceptor as well as effectively separating electrons and holes. The intermediates generated during the TC degradation in the photo-Fenton process were detected by HPLC-MS, which proved that the holes, superoxide radicals, and singlet oxygen are the key reactive species in the Fenton-like photocatalysis. This study provides a new option for the treatment of TC in wastewater.

Keywords: Fenton-like photocatalysis; Co-CNK-OH; tetracycline; reactive oxygen species



Citation: Hou, D.; Luo, J.; Sun, Q.; Zhang, M.; Wang, J. Preparation of Co-CNK-OH and Its Performance in Fenton-like Photocatalytic Degradation of Tetracycline. *Catalysts* **2023**, *13*, 715. <https://doi.org/10.3390/catal13040715>

Academic Editors: Jiangkun Du, Lie Yang and Chengdu Qi

Received: 7 March 2023

Revised: 2 April 2023

Accepted: 5 April 2023

Published: 9 April 2023



Copyright: © 2023 by the authors. Licensee MDPI, Basel, Switzerland. This article is an open access article distributed under the terms and conditions of the Creative Commons Attribution (CC BY) license (<https://creativecommons.org/licenses/by/4.0/>).

1. Introduction

In recent years, an endless variety of antibiotics has been synthesized and manufactured as therapeutic drugs to treat infectious diseases in humans, animals, and even plants around the world [1]. Antibiotic-induced sewage pollution is highly concerned as a large quantity of antibiotics has entered water bodies with the widespread application of antibiotics. Tetracycline (TC), which is widely used to treat diseases in livestock animals, is difficult to degrade in nature, resulting in the continuous release and accumulation of TC in the natural water environment [2,3]. Therefore, it is urgent to develop more effective methods for degrading tetracycline in wastewater treatment technologies.

Common methods used to degrade TC fall into several categories, such as biological treatment, adsorption and desorption, membrane treatment, and advanced oxidation technologies [4–7]. Among the advanced oxidation technologies, the Fenton process is currently a popular method of water-pollution treatment. However, the classical Fenton process has many limitations on its practical applications, such as a relatively narrow pH range and heavy iron deposition, leading to increased treatment costs and low efficiency in the utilization of H₂O₂ [8,9]. Thus, Fenton-like technologies have increasingly become alternative choices [10–12].

Graphite-like carbon nitride (g-C₃N₄), a common two-dimensional (2D) material, has attracted extensive research attention in the field of photocatalysis because of its non-toxicity, low cost, good stability, and visible-light response [13–15]. Moreover, g-C₃N₄ can stimulate the generation of hydroxyl radicals (\cdot OH) from H₂O₂ and is often used as a Fenton-like catalyst [16]. However, the rapid recombination of electron-hole pairs in g-C₃N₄ limits its application on the degradation of organic pollutants [17]. To solve this

problem, Thi Quyen et al. [18] improved the light absorption behavior by doping S in $g\text{-C}_3\text{N}_4$, which can effectively reduce the recombination rate of electron–hole pairs in $g\text{-C}_3\text{N}_4$. Bao et al. [19] prepared Cu-doped $g\text{-C}_3\text{N}_4$ by a simple template-mediated supramolecular-self-assembly method, in which the specific surface area of the $g\text{-C}_3\text{N}_4$ was considerably increased while achieving enhanced light absorption and higher separation and transfer efficiency of the photogenerated carriers. The energy bandgap in $g\text{-C}_3\text{N}_4$ can be adjusted by doping with metallic or nonmetallic elements to prevent the recombination of electrons and holes [14,18–22]. Alkalinization treatment is an important surface/interface modulation tool to reduce the energy bandgap by grafting hydroxyl groups, which can inhibit the recombination of photogenerated electrons and holes and improve the Fenton-like catalytic activity, with limited improvement in the photocatalytic performance [23–25]. The combination of alkalinization treatment and metal-ion modification can effectively enhance the performance of photocatalysis. For example, Cong et al. [26] improved the specific surface area and electrochemical activity by embedding Co ions in $g\text{-C}_3\text{N}_4$, and the produced Co- $g\text{-C}_3\text{N}_4$ showed excellent catalytic performance in the PMS-activated degradation of TC.

To the best of our knowledge, a Co-doped $g\text{-C}_3\text{N}_4$ alkalinized catalyst has never been reported. In this work, a novel Co^{2+} -doped $g\text{-C}_3\text{N}_4$ alkalinized catalyst (Co-CNK-OH) was prepared by a simple calcination–impregnation approach. On the one hand, the basic treatment can transplant numerous hydroxyl groups on the surface of the $g\text{-C}_3\text{N}_4$ to generate active hydroxyl radicals and decrease the energy bandgap of the $g\text{-C}_3\text{N}_4$. On the other hand, the doping of metal ions can significantly improve the Fenton-like catalytic activity of the $g\text{-C}_3\text{N}_4$ through the variable valence state of the metal ions. Compared with similar products, the Co-CNK-OH catalyst exhibits superior degradation performance for TC under visible-light irradiation. This study provides a new option for the treatment of tetracycline in wastewater.

2. Results

2.1. Characterization of As-Prepared Samples

Figure 1a shows the XRD spectra of the as-prepared $g\text{-C}_3\text{N}_4$, CNK-OH, and Co-CNK-OH heterojunctions with different Co contents. Two typical characteristic peaks for $g\text{-C}_3\text{N}_4$ were found at 13.0° and 27.4° , corresponding to the (100) and (200) crystal planes of the $g\text{-C}_3\text{N}_4$, respectively [27]. The (100) plane at 13.0° disappeared compared with that of the pure $g\text{-C}_3\text{N}_4$ when the $g\text{-C}_3\text{N}_4$ was alkalinized with KCl and NH_4Cl , implying that K^+ ions were embedded into the $g\text{-C}_3\text{N}_4$ plane and an attraction force between K and N atoms. This was consistent with the results of the K 2p XPS spectra [28]. As for the (200) plane, a slight shift in the peak from 27.4° to 28.1° for the CNK-OH indicated a smaller interlayer spacing of the (200) plane in the CNK-OH [16]. The intensity of the diffraction peak gradually decreased with increasing Co^{2+} content, indicating that Co^{2+} was successfully doped in the framework of the $g\text{-C}_3\text{N}_4$ and that the Co-doping partly damaged the in-plane structure of the $g\text{-C}_3\text{N}_4$ [29]. The XRD diffraction peak of the CNK-OH was basically unchanged, even with Co^{2+} ions loading, indicating that Co^{2+} ions might have been embedded in the center of the triazine ring unit [30,31].

FT-IR was used to investigate the chemical structures and compositions of the $g\text{-C}_3\text{N}_4$, CNK-OH, and 9%Co-CNK-OH materials (Figure 1b), and characteristic peaks at 800 cm^{-1} and between 1200 and 1700 cm^{-1} were observed for all the samples. The peak at 800 cm^{-1} was attributed to the typical vibration of the repeating triazine unit. The absorption band at $1200\text{--}1700\text{ cm}^{-1}$ could be assigned to the stretching vibrations of the aromatic CN heterocycles in the $g\text{-C}_3\text{N}_4$ [32]. Compared with the peaks for the $g\text{-C}_3\text{N}_4$, three additional peaks appeared at $\sim 994\text{ cm}^{-1}$, 1148 cm^{-1} , and 2180 cm^{-1} for the CNK-OH and 9%Co-CNK-OH by the introduction of K^+ ions. The peaks at 994 cm^{-1} and 1148 cm^{-1} corresponded to the vibrational modes of the O-H and C-O or C=O bonds, respectively, verifying that hydroxyl groups were effectively grafted on the surface of the $g\text{-C}_3\text{N}_4$ by this alkalinization modification method [27]. The band at 2180 cm^{-1} belonged to the cyano

group (C≡N), which suggested that the introduction of K⁺ ions ruptured the C-N-C bonds in the g-C₃N₄ to form new C≡N bonds [16]. The FT-IR spectrum of the 9%Co-CNK-OH sample was similar to that of the CNK-OH sample, and no evident change was found because of the metal modification.

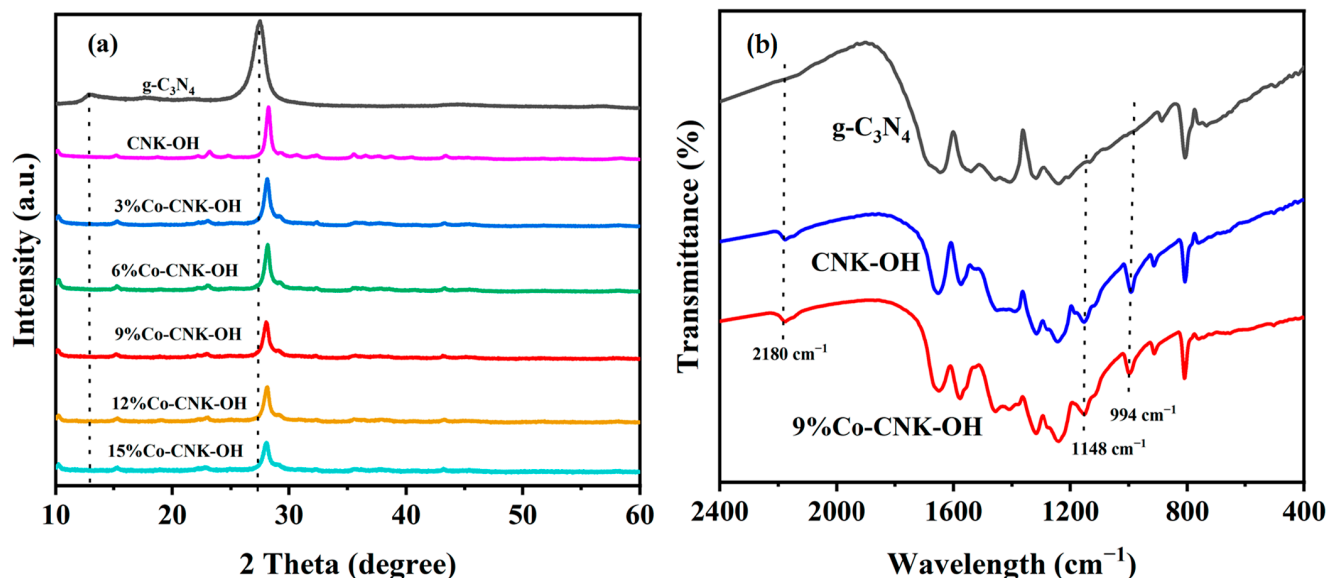


Figure 1. The XRD patterns of g-C₃N₄, CNK-OH and Co-CNK-OH (a) and FT-IR spectra of g-C₃N₄, CNK-OH, and 9%Co-CNK-OH (b).

2.2. Morphology and Structural Properties

To investigate the microstructures of the g-C₃N₄, CNK-OH, and 9%Co-CNK-OH materials, SEM and TEM images of the as-prepared samples are shown in Figure 2a–f.

To confirm the elemental distribution, the EDS and elemental mapping images of the Co-CNK-OH are shown (Figure 3a–g). It was obvious that the surface of the g-C₃N₄ was smooth while the surface of the CNK-OH became rougher with dispersed particles after the alkalization treatment (Figure 2a,b), which may have been due to the influence of the grafted hydroxyl group on the surface of the g-C₃N₄ [33]. Compared with the CNK-OH and g-C₃N₄ surfaces, smaller solid particles were observed, and the surface of the Co-CNK-OH was much rougher after the Co²⁺ modification (Figure 2c). From the microstructure of the CNK-OH, numerous nanosheets on the surface could be clearly seen (Figure 2e). However, the modification with Co²⁺ resulted in a more fragmented and uniformly dispersed nanosheet structure, in agreement with the SEM analysis results (Figure 2e,f). As for Co-CNK-OH, it was clear that C, N, O, K, and Co were uniformly distributed on the surface of the Co-CNK-OH material in Figure 3c–g, and the previously mentioned evidence implied the formation of Co-CNK-OH heterojunctions at the microscopic level.

To clarify the detailed chemical bonding and valence states of the constituent elements in Co-CNK-OH, the XPS spectra of the 9%Co-CNK-OH show the peaks of C 1s, N 1s, O 1s, K 2p, and Co 2p (Figure 4a). In the spectrum of C 1s (Figure 4b), the characteristic peaks at binding energy (BE) = 288.43 and 284.79 eV correspond to the N=C=N group and C=C bond of the g-C₃N₄, respectively [34]. The weak peak at 286.27 eV was due to the C-OH group [31], confirming the grafting of the hydroxyl groups on the surface of the g-C₃N₄. Four characteristics peaks at 398.33, 400.90, 403.79, and 404.54 eV were found in the N 1s spectrum (Figure 4c). The characteristic peaks at 398.33, 400.90, and 403.79 eV could be ascribed to the C-N=C, N-(C)₃, and C-N-H groups in the g-C₃N₄, respectively [14,35], while the peak at 404.54 eV was caused by the delocalization of the π -electrons in the g-C₃N₄ [31]. In the O 1s spectrum (Figure 4d), two peaks were fitted, in which the peak at 532.52 eV was assigned to the binding of water molecules, while the peak at 531.11 eV belonged to the OH bond [31,36], which further proved the implantation of the hydroxyl

group in the $g\text{-C}_3\text{N}_4$. The K 2p spectrum depicts two characteristic peaks. The peak at 293.08 eV could be attributed to the N-K bond (Figure 4e), such as that in KN_3 , indicating that K^+ ions can break the C-N bond in $g\text{-C}_3\text{N}_4$ and insert into the plane of $g\text{-C}_3\text{N}_4$ by the mutual attraction between the K and N atoms. This is crucial to the subsequent grafting of the surface hydroxyl groups, in accordance with the results of the FTIR [16]. As for the spectrum of Co 2p (Figure 4f), the characteristic peaks at 780.88 and 796.63 eV were the main peaks of Co $2p_{3/2}$ and Co $2p_{1/2}$, respectively; BE of Co $2p_{1/2}$ (796.63 eV) was lower than that of metallic cobalt (799 eV) while BE of Co $2p_{3/2}$ (780.88 eV) was higher than that of cobalt oxide (779–780 eV), suggesting that the doped Co^{2+} ions combined with the N atoms in the $g\text{-C}_3\text{N}_4$ to form Co-N bonds [37–39]; the peaks at 784.34, 787.85, and 802.41 eV are satellite peaks, representing the vibrations of the Co^{2+} ions [26,40,41]. From the combined results of the XRD, FT-IR, SEM, TEM, EDS, and XPS, it was concluded that Co^{2+} ions were doped in CNK-OH.

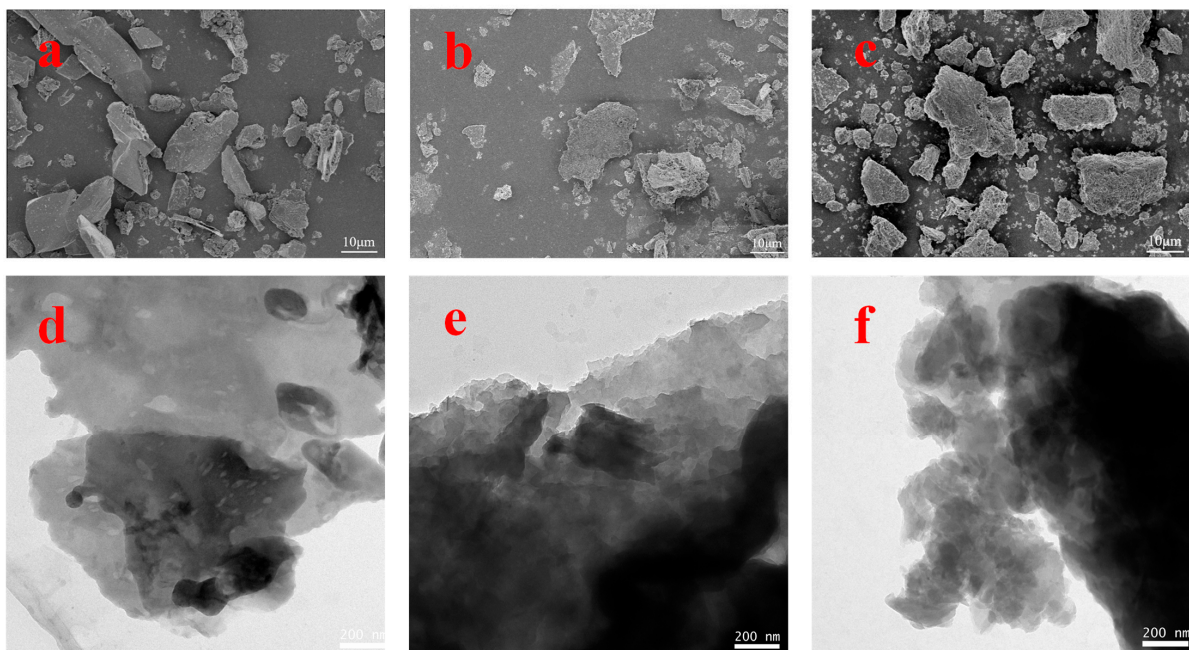


Figure 2. SEM images of $g\text{-C}_3\text{N}_4$ (a), CNK-OH (b), Co-CNK-OH (c) and TEM images of $g\text{-C}_3\text{N}_4$ (d), CNK-OH (e), and 9%Co-CNK-OH (f).

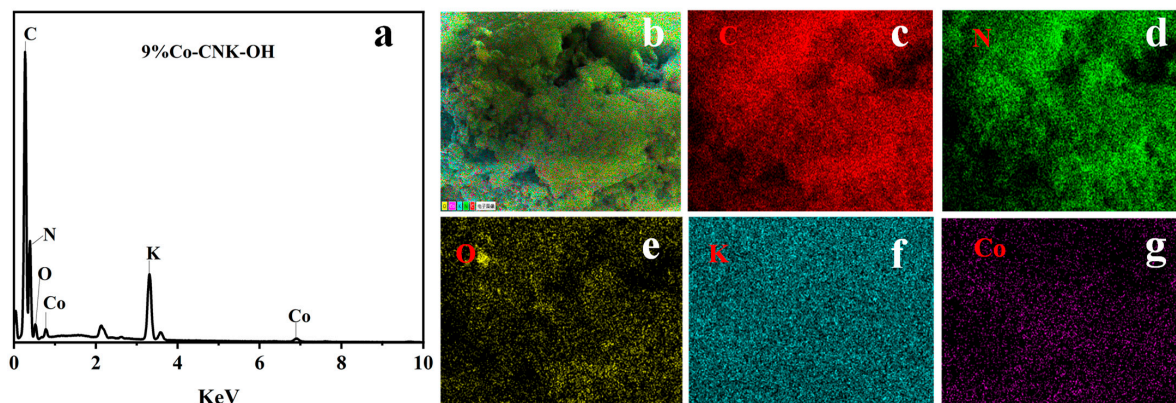


Figure 3. EDS of 9%Co-CNK-OH (a) and the elemental mapping images of 9%Co-CNK-OH (b–g).

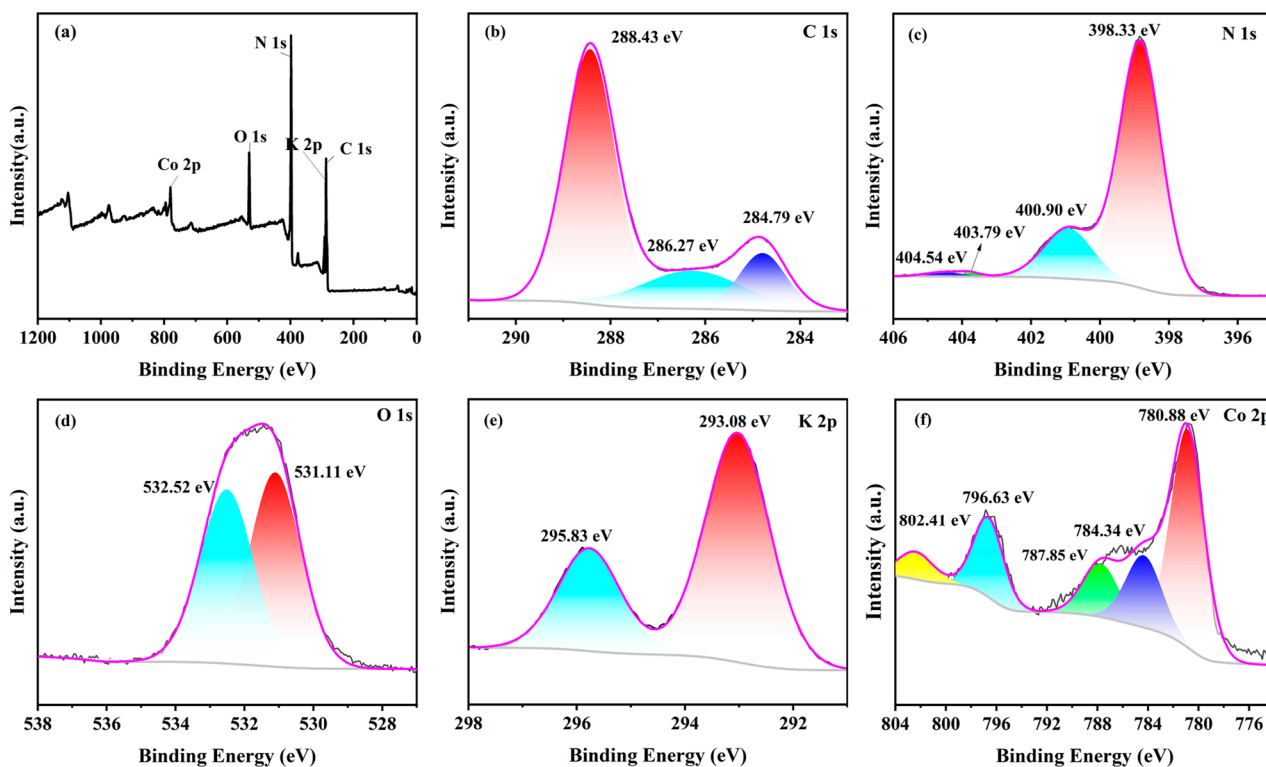


Figure 4. The XPS spectra of 9%Co-CNK-OH: (a) full spectrum, (b) C 1s, (c) N 1s, (d) O 1s, (e) K 2p, and (f) Co 2p.

The N_2 adsorption–desorption isotherms and corresponding pore-size-distribution curves of the $g-C_3N_4$, CNK-OH, and 9%Co-CNK-OH were further analyzed (Figure 5), and all the samples belonged to type IV [42].

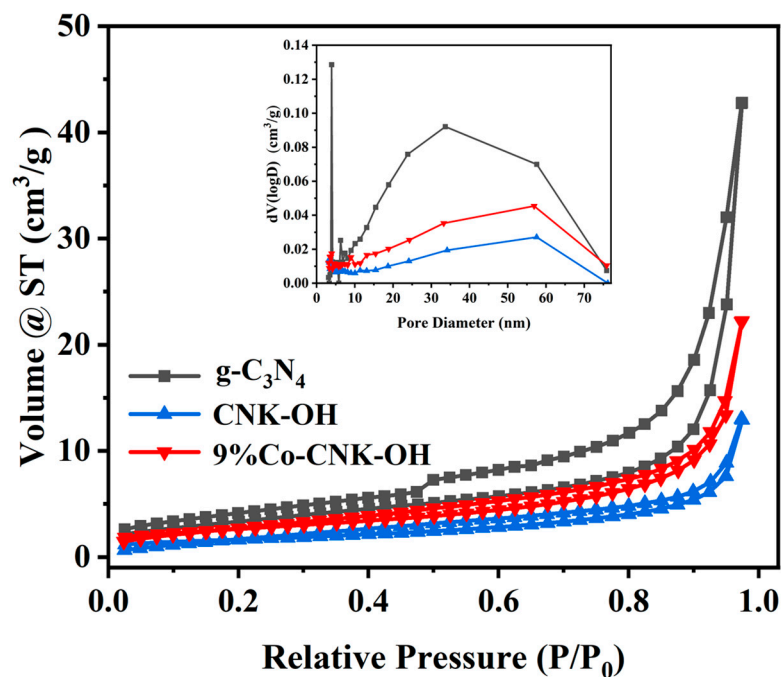


Figure 5. Nitrogen adsorption-desorption isotherms (outer figure) and corresponding pore-size distribution curves (sub-figure) for $g-C_3N_4$, CNK-OH and 9%Co-CNK-OH.

From Table 1, g-C₃N₄, CNK-OH, and 9%Co-CNK-OH had specific surface areas of 15.279, 5.146, and 8.243 m²/g, respectively. The specific surface area of CNK-OH was smaller than that of g-C₃N₄, which could be attributed to the mixing of KCl with the g-C₃N₄ samples, whereby K⁺ ions entered into g-C₃N₄ to inhibit N₂ adsorption and partially block the mesopores [24]; however, a slightly increased specific surface area was obtained after Co²⁺ loading.

Table 1. Specific surface areas and pore-size parameters of g-C₃N₄, CNK-OH and 9%Co-CNK-OH.

Sample	S _{BET} (m ² g ⁻¹)	Pore Volume (cm ³ g ⁻¹)	Average Pore Size (nm)
g-C ₃ N ₄	15.279	0.066	3.924
CNK-OH	5.416	0.019	3.130
9%Co-CNK-OH	8.243	0.033	3.926

2.3. Optical and Photoelectric Properties

The optical properties of the catalysts were measured by the UV-Vis diffuse reflectance spectra (Figure 6a).

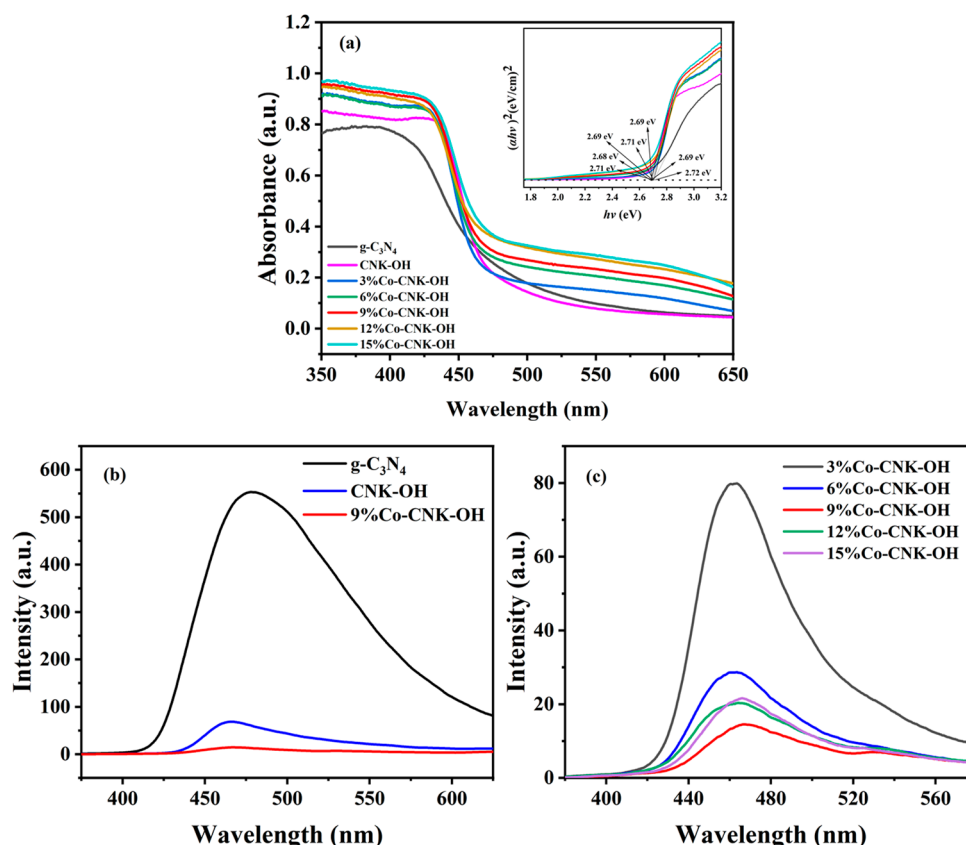


Figure 6. UV-vis diffuse reflectance patterns of g-C₃N₄, CNK-OH and Co-CNK-OH (outer figure), plots of $(ahv)^2$ versus $h\nu$ of g-C₃N₄, CNK-OH and Co-CNK-OH (sub-figure) (a); PL emission spectra of g-C₃N₄, CNK-OH, and 9%Co-CNK-OH (b); and PL emission spectra of X%Co-CNK-OH (c).

The absorption edge of g-C₃N₄ was located at about 460 nm, with a large bandgap energy of about 2.7 eV. Compared with the g-C₃N₄ and CNK-OH absorption edges, those of all the Co-CNK-OH catalysts with different Co contents shifted slightly toward the long-wave range, and the intensities of the visible-light absorbance were increased by the Co²⁺ modification. The E_g values of the g-C₃N₄, CNK-OH, and Co-CNK-OH were deduced from the linear extension of the $(ahv)^2$ versus $h\nu$ curve to the X-axis. The E_g values of g-

C_3N_4 , CNK-OH, 3%Co-CNK-OH, 6%Co-CNK-OH, 9%Co-CNK-OH, 12%Co-CNK-OH, and 15%Co-CNK-OH were 2.71, 2.69, 2.72, 2.71, 2.68, 2.69, and 2.69 eV, respectively (Table 2).

Table 2. E_g , E_{FB} , E_{CB} , and E_{VB} of $g-C_3N_4$, CNK-OH and Co-CNK-OH.

Sample	E_g (eV)	E_{FB} (V vs. Ag/AgCl)	E_{CB} (V vs. NHE)	E_{VB} (V)
$g-C_3N_4$	2.71	−0.437	−0.24	2.47
CNK-OH	2.69	−0.458	−0.261	2.429
3%Co-CNK-OH	2.72	−0.486	−0.289	2.231
6%Co-CNK-OH	2.71	−0.433	−0.236	2.474
9%Co-CNK-OH	2.68	−0.487	−0.29	2.39
12%Co-CNK-OH	2.69	−0.427	−0.23	2.46
15%Co-CNK-OH	2.69	−0.374	−0.187	2.503

PL emission spectroscopy is an effective method to detect the combination of photo-generated electrons and holes. The fluorescence intensity of $g-C_3N_4$ was very strong, while the fluorescence intensity of the CNK-OH modified by alkalization was sharply reduced to about 1/8 of that of $g-C_3N_4$ (Figure 6b, c). The PL intensity of Co-CNK-OH further decreased compared with that of CNK-OH, indicating that the introduction of Co^{2+} ions could effectively promote the separation of electrons and holes. The PL intensity of 9%Co-CNK-OH reached the minimum value and then PL intensity increased instead while further increasing the Co content, suggesting that the optimum dopant was 9%Co-CNK-OH for the most efficient separation of electron–hole pairs.

Mott–Schottky curves were applied to detect the type of semiconductor. As shown in Figure 7, the observed curves of all the samples show significantly positive slopes, indicating that $g-C_3N_4$, CNK-OH, and Co-CNK-OH were all categorized as n-type semiconductors. As listed in Table 2, the E_{FB} and E_{VB} of $g-C_3N_4$, CNK-OH, and Co-CNK-OH were calculated by extending the linear part of $C^{-2} = 0$ to obtain E_{FB} , $E_{CB} = E_{FB} + 0.197$ V (the standard electrode potential of Ag/AgCl), and $E_{VB} = E_g + E_{CB}$ [16].

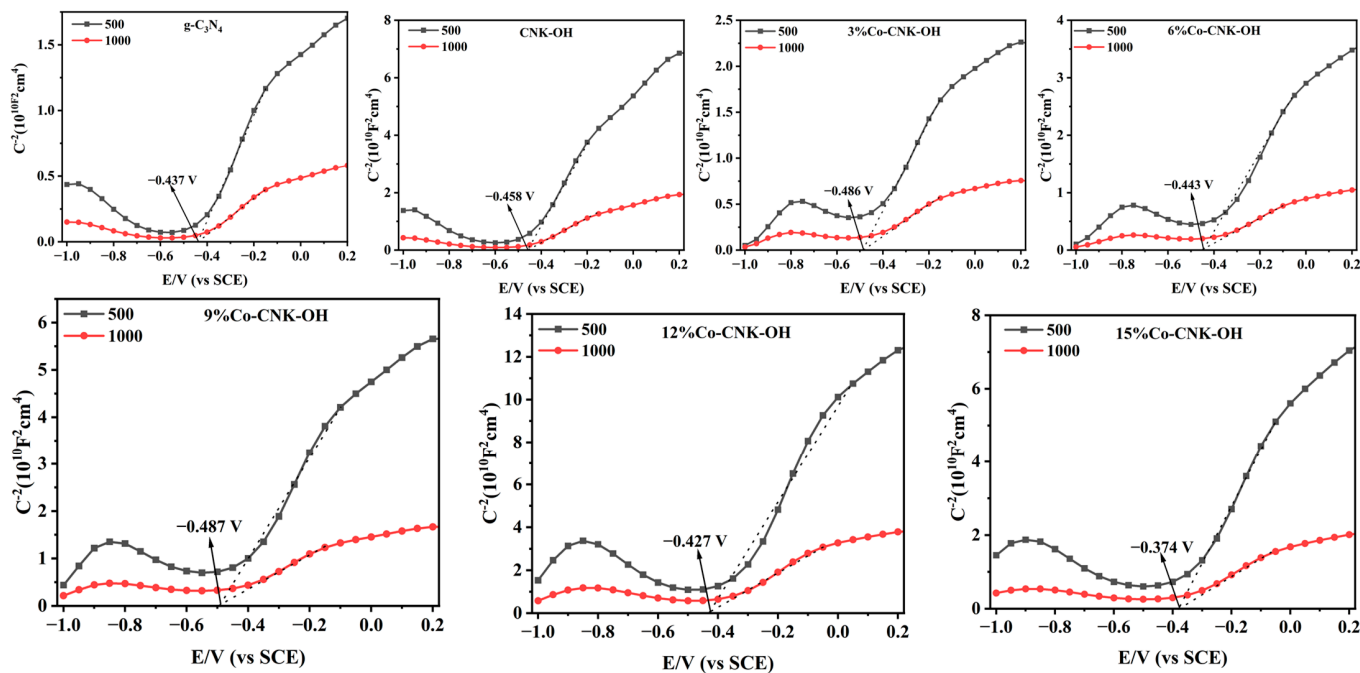


Figure 7. Mott–Schottky curves of $g-C_3N_4$, CNK-OH, and Co-CNK-OH.

Electrochemical impedance spectroscopy (EIS) is commonly used to probe the separation efficiency of electrons and resistance to interfacial charge transfer of semiconductor materials. The EIS curves of g-C₃N₄, CNK-OH, and Co-CNK-OH are shown in Figure 8. The arc radius of 9%Co-CNK-OH was significantly smaller than those of the other samples, implying that the electrical resistance of 9%Co-CNK-OH was the lowest, in accordance with the best electron-transfer performance and suggesting that Co²⁺ modification significantly promote the interfacial charge to the electron acceptor and separate electrons and holes effectively [43].

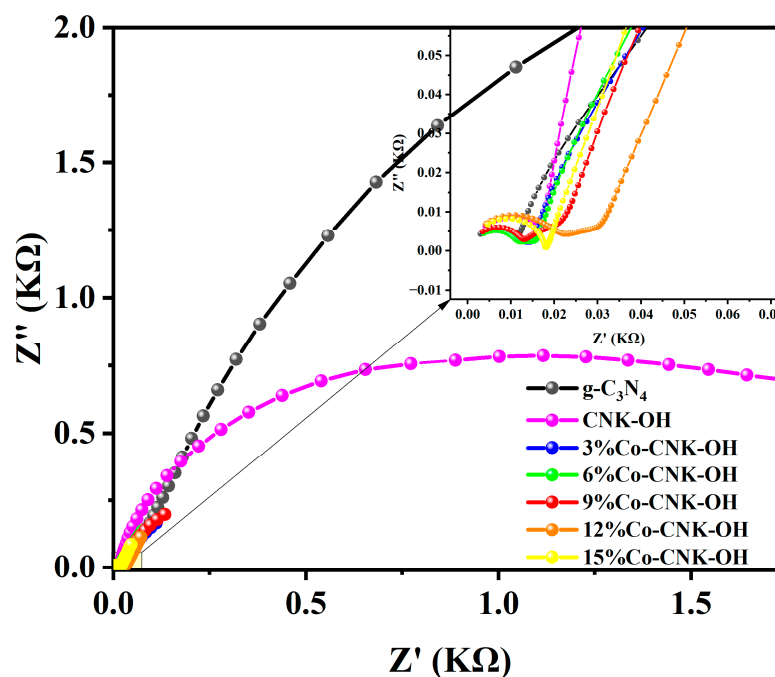


Figure 8. EIS of g-C₃N₄, CNK-OH, and Co-CNK-OH (outer figure) and enlarged view of 0.00–0.07 KΩ (sub-figure).

2.4. Catalytic Performance and Mechanism of As-Prepared Samples

In order to evaluate the catalytic performance of Co-CNK-OH, the optimal experiments were designed, and the results are shown in Figure S1. From Figure S1, the optimal reaction conditions for the TC degradation were as follows: the amount of catalyst was 50 mg L^{−1}, the concentration of H₂O₂ was 30 mM, pH = 7, and the initial concentration of the TC was 20 mg L^{−1}. Different reaction systems were applied to TC degradation. As shown in Figure 9a, with visible light alone or with visible light and H₂O₂, only a slight self-degradation of the TC occurred in 40 min. Adding g-C₃N₄ and CNK-OH led to the degradation efficiency of TC reaching 25.30 and 47.45%, respectively, indicating that the alkalinized g-C₃N₄ promoted the degradation of TC because of the introduction of hydroxyl groups. It was noteworthy that the Co modification enhanced the degradation efficiency of TC by Co-CNK-OH. In detail, the degradation efficiency of TC increased with increasing Co content (3–9%) and then decreased with further increases in the Co content, which could be explained by the introduction of defects that act as a complex center for the charge carriers [44]. The highest-efficiency TC degradation with 9%Co-CNK-OH was 87.10% in 40 min. The leaching of Co²⁺ ions after catalysis was also investigated by inductively coupled plasma mass spectrometry (ICP-MS). The result of the ICP-MS indicated that the concentration of the free Co²⁺ in the solution after the reaction was 0.21 mg/L, which complies with China’s emission standards for copper, cobalt, and nickel industrial sources (GB25467-2010, 1 mg/L).

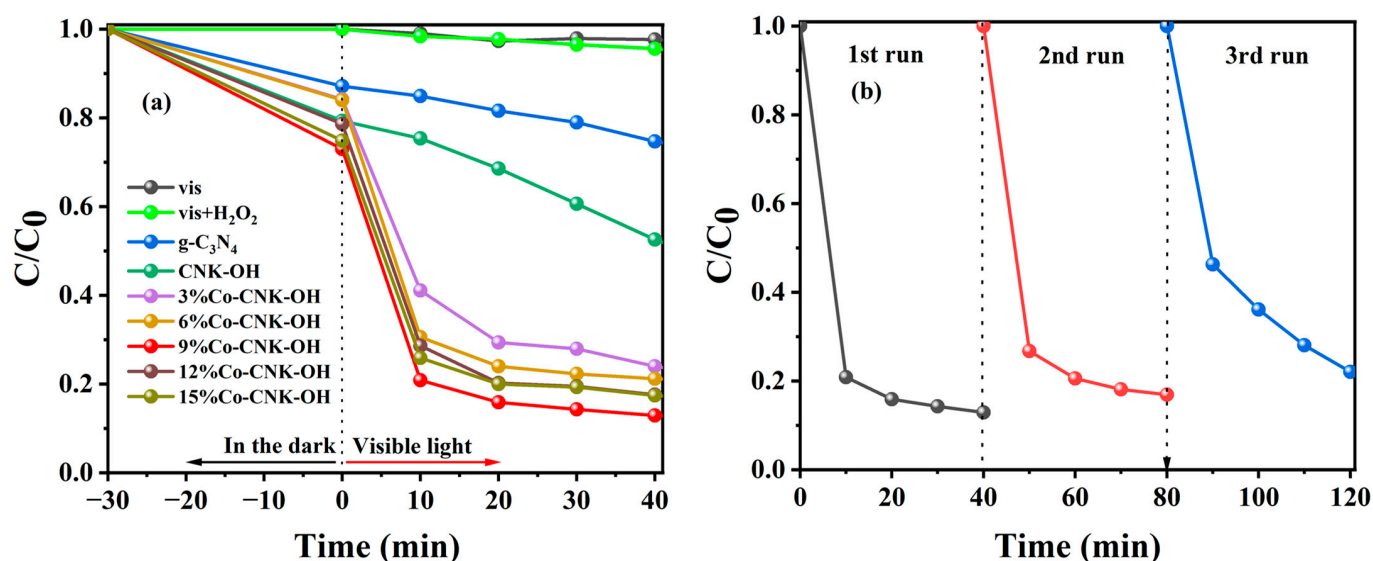


Figure 9. Degradation curves of TC in different reaction systems (a), cycle test of 9%Co-CNK-OH for TC degradation (b). Reaction conditions: catalyst dosage: 50 mg L⁻¹, H₂O₂: 30 mM, pH: 7, and TC: 20 mg L⁻¹.

The reusability and stability of the catalyst are critical for practical applications. In order to evaluate the durability of the catalysts, three cycles of repeated experiments were carried out with 9%Co-CNK-OH under similar conditions (Figure 9b). It could be observed that the degradation efficiency of TC decreased from 87.1% to 77.95%, suggesting that the Co-CNK-OH sample had excellent stability.

To monitor the effect of the mineralization property of the photocatalyst on organic pollutants, the TOC removal efficiency of TC by the 9%Co-CNK-OH catalyst under visible-light irradiation was investigated (Figure 10a). The TOC removal efficiency of the TC by the 9%CO-CNK-OH catalyst was 50% after 60 min. The mineralization property of the 9%Co-CNK-OH catalyst is better than some previous reports (41%) [45].

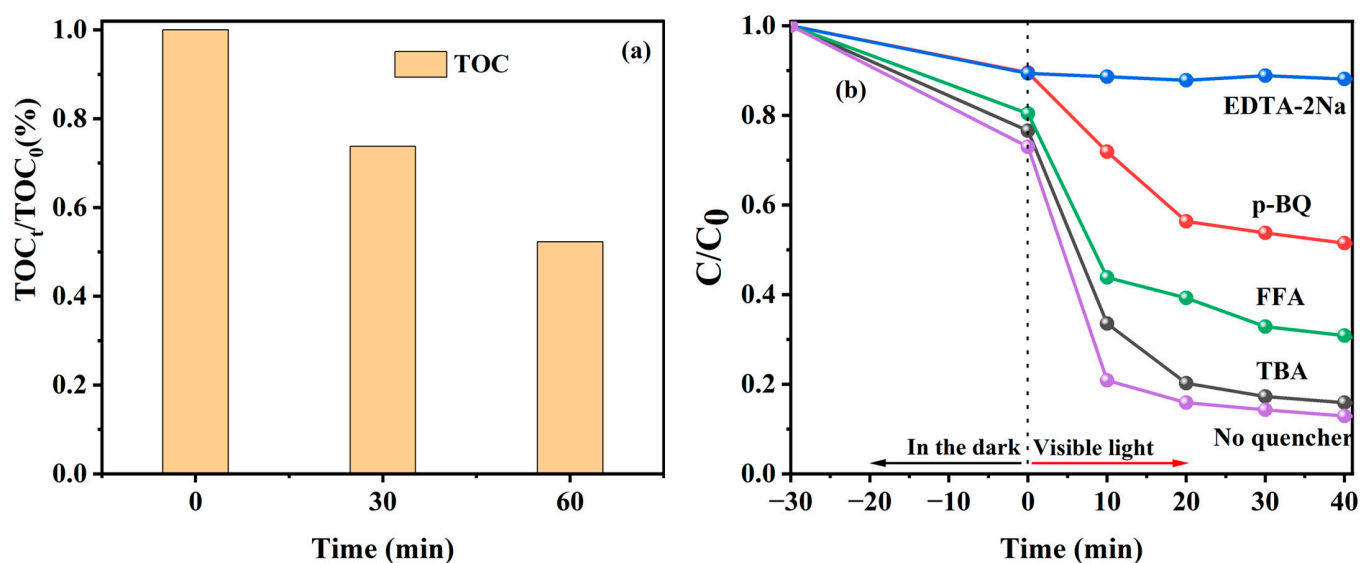


Figure 10. TOC changes in TC by 9%Co-CNK-OH under visible light (a); photo-Fenton degradation efficiencies of TC by 9%Co-CNK-OH with different scavengers under visible light (b).

To figure out the mechanism of TC degradation by 9%Co-CNK-OH, TBA, EDTA-2Na, p-BQ, and FFA were used to capture $\cdot\text{OH}$, h^+ , $\cdot\text{O}_2^-$ and $^1\text{O}_2$, respectively (Figure 10b). Compared with the efficiency of TC removal (87.10%) by 9%Co-CNK-OH without any

trapping-agent addition, the efficiency of TC degradation was reduced by 2.95%, 75.25%, 38.60%, and 17.98% with the addition of TBA, EDTA-2Na, p-BQ, and FFA, respectively, suggesting that h^+ , $\cdot O_2^-$, and 1O_2 are the main active species for the photocatalytically assisted Fenton-like degradation of TC by Co-CNK-OH.

The possible intermediates generated during TC degradation in the photo-Fenton process were investigated by HPLC-MS, as well as the possible TC-degradation pathway by 9%Co-CNK-OH (Figures 11 and 12). The main intermediates were named P1 ($m/z = 441$), P2 ($m/z = 417$), P3 ($m/z = 407$), P4 ($m/z = 256$), P5 ($m/z = 352$), P6 ($m/z = 338$), P7 ($m/z = 240$), P8 ($m/z = 186$), P9 ($m/z = 117$), etc. First, the TC molecules were attacked by reactive substances (h^+ , $\cdot O_2^-$, 1O_2 or $\cdot OH$) to form P1 ($m/z = 441$), P2 ($m/z = 417$), and P3 ($m/z = 407$) [46]. P1 ($m/z = 441$) was produced by demethylation and then reacted to form P4 ($m/z=256$) by dehydroxylation, deamidation, and ring-opening reactions. P2 ($m/z = 417$) lost amine and carbonyl groups by the deamidation reaction to produce P5 ($m/z = 352$) [47]. Then, P5 was further attacked by free radicals to form P6 ($m/z = 338$) by the rupture of the cyclic hydrocarbon [48], followed by the ring-opening reaction due to the action of $\cdot O_2^-$ to produce P7 ($m/z = 240$) with the loss of methanol [49]. P8 ($m/z = 186$) was obtained by the ring-opening reaction and dihydroxylation of P7 ($m/z = 240$) [22]. Another possibility is that P6 ($m/z = 338$) underwent demethylation and hydroxylation to produce P9 ($m/z = 117$). Finally, these smaller molecules can be completely mineralized to produce H_2O and CO_2 or other molecules.

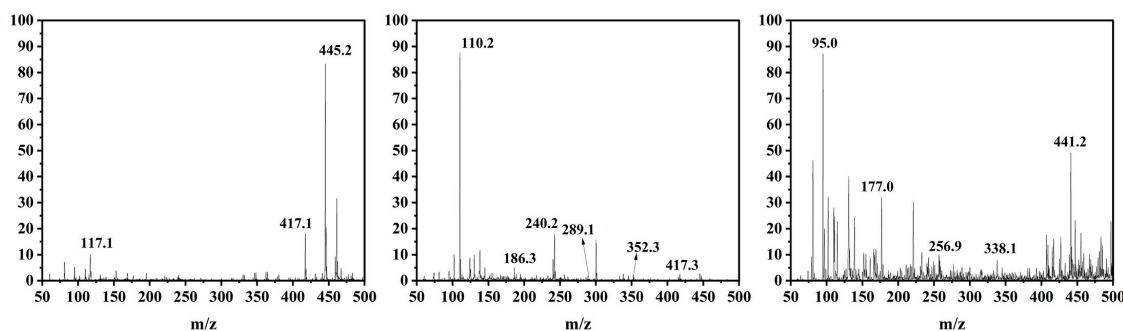
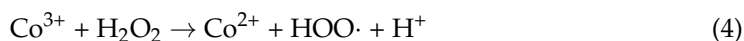
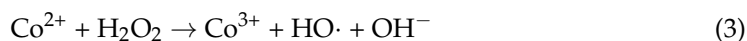


Figure 11. Mass spectra of tetracycline and its corresponding intermediates during photo-Fenton degradation of TC.

In view of this analysis, a possible mechanism for TC degradation by 9%Co-CNK-OH catalyst is proposed (Figure 13). First, numerous photogenerated electrons and holes in the conduction and valence bands were generated under visible-light irradiation and an internal electric field for the 9%Co-CNK-OH samples and $\cdot O_2^-$ was formed. The addition of H_2O_2 promoted the formation of both 1O_2 and $\cdot O_2^-$. The Co (III)/Co (II) redox cycle accelerated the consumption of the photogenerated electrons and then promoted the separation of the photogenerated electrons and holes while keeping the continuous generation of 1O_2 , $\cdot O_2^-$, and h^+ in the system [50,51]. Therefore, TC degradation by 9%Co-CNK-OH was attributed to the synergistic effect of photocatalysis and Fenton reactions. The possible reactions are listed as follows:



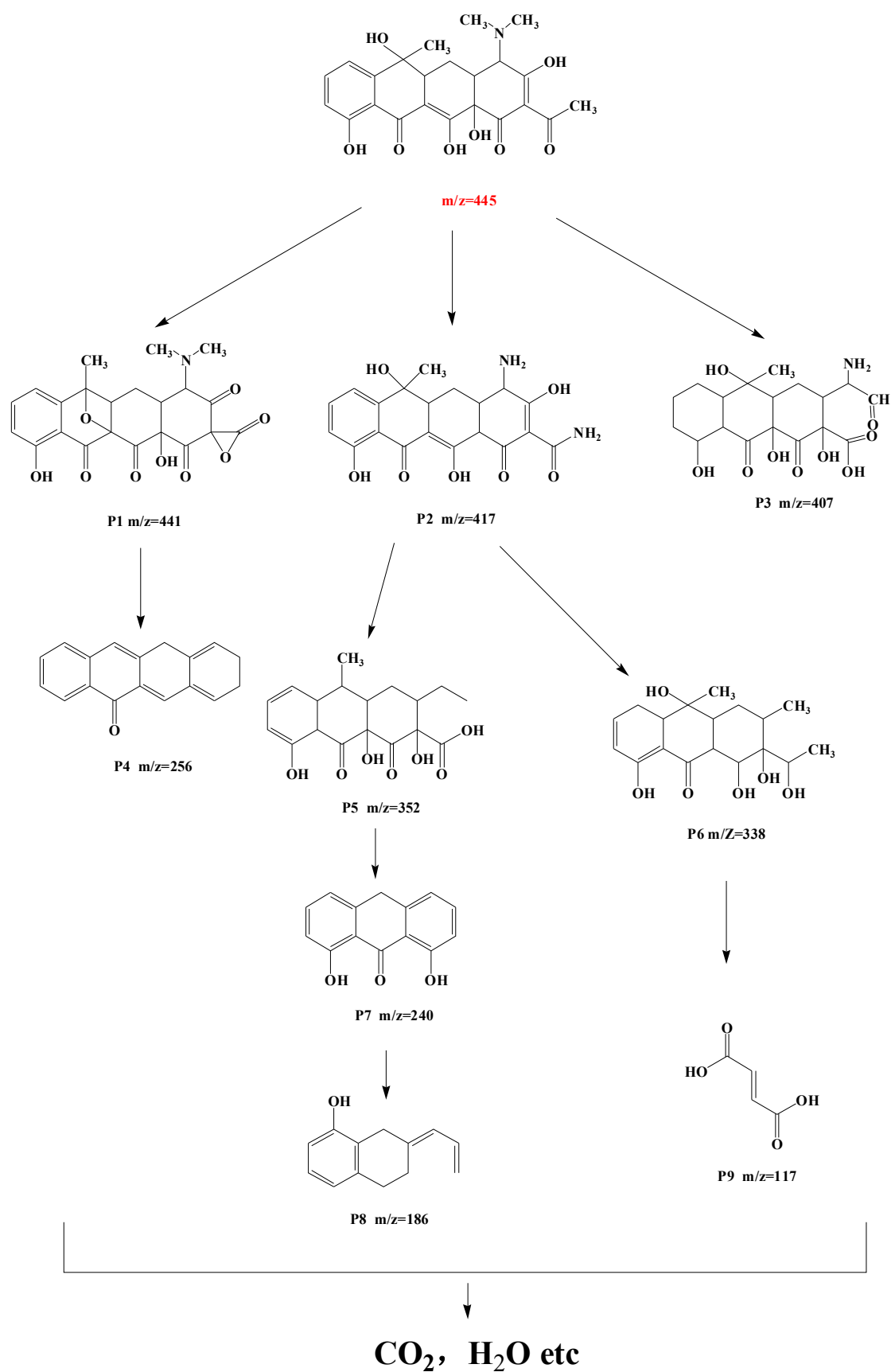


Figure 12. Possible TC degradation pathway by 9%Co-CNK-OH.

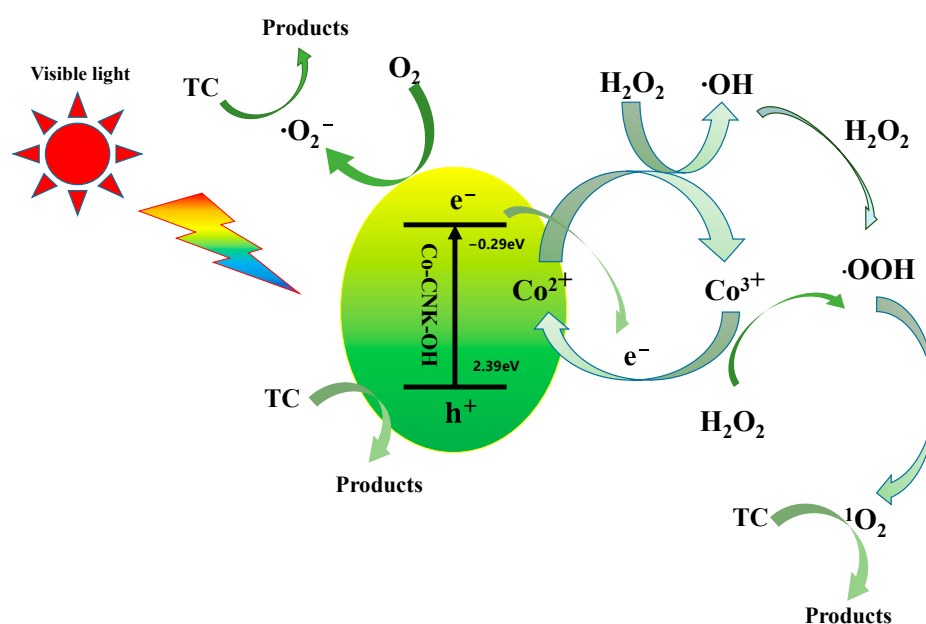


Figure 13. Possible photocatalytic mechanism of TC degradation by Co-CNK-OH in Fenton-like photocatalytic systems.

3. Materials and Methods

3.1. Chemicals

Melamine ($\text{C}_3\text{H}_6\text{N}_6$, 99%) and furfuryl alcohol ($\text{C}_5\text{H}_6\text{O}_2$, 98%) were purchased from Aladdin Chemistry Co., Ltd. (Shanghai, China). Potassium chloride (KCl, 99.5%), ethylenediaminetetraacetic acid disodium salt (EDTA-2Na), and cobalt chloride hexahydrate ($\text{CoCl}_2 \cdot 6\text{H}_2\text{O}$, 99%) were purchased from Comeo Chemical Reagent Co., Ltd. (Tianjin, China). Ammonium chloride (NH_4Cl , 99.5%) was purchased from Fengfan chemical reagent technology Co., Ltd. (Tianjin, China). Tetracycline (TC) was purchased from Macklin Biochemical Co., Ltd. (Shanghai, China). Hydrochloric acid (HCl, 36–38%) was provided by Haohua chemical reagent Co., Ltd. (Luoyang, China), and p-benzoquinone (p-BQ) was purchased from Sinopharm Chemical Reagent Co., Ltd. (Beijing, China). Tert-butanol (t-BuOH, 99.8%) was provided by Yong chemical reagent Co., Ltd. (Tianjin, China). Hydrogen peroxide (H_2O_2 , 30%) was obtained from Xilong Chemical Co., Ltd. (Shantou, China). All chemical reagents were used without any purification.

3.2. Materials Synthesis

3.2.1. Preparation of CNK-OH

The steps for preparing alkalized g- C_3N_4 (CNK-OH) were the same as those followed by Li. First, 9 g of melamine, 45 g of KCl, and 0.6 g of NH_4Cl were mixed and ground thoroughly in a mortar for 30 min. Then, the mixture was transferred to a ceramic crucible, heated to 550 °C at 2.3 °C/min in a muffle furnace, kept there for 4 h, and cooled naturally in the air. The obtained solid was ground into powder, dissolved in 200 mL of

deionized water, stirred for 6 h, washed by vacuum filtration, dried in an oven at 80 °C for 12 h, and ground again to obtain the as-prepared CNK-OH. Under the same conditions, pure g-C₃N₄ was prepared with 4.5 g of melamine but without KCl or NH₄Cl.

3.2.2. Fabrication of Co-CNK-OH Composites

Co-CNK-OH composites were prepared by an impregnation method [16]. First, 0.48 g of CNK-OH was dispersed in 100 mL of deionized water (denoted as solution A); a certain amount of CoCl₂·6H₂O was dissolved in 100 mL of deionized water (denoted as solution B). Then, solution B was added dropwise to solution A while stirred slowly, then stirred for 36 h at room temperature. The obtained suspension was sonicated for 3 h, washed three times each with deionized water and ethanol, and dried in an oven at 80 °C for 12 h to obtain the as-prepared Co-CNK-OH sample. The mass ratios of CoCl₂·6H₂O and CNK-OH were designed between 3 and 15%, and the Co-CNK-OH samples loaded with different Co contents are expressed as weight percentages of Co-CNK-OH for simplicity. Accordingly, 3%Co-CNK-OH, 6%Co-CNK-OH, 9%Co-CNK-OH, 12%Co-CNK-OH, and 15%Co-CNK-OH samples were prepared.

3.3. Degradation Experiments

First, a certain amount of the as-prepared catalyst was dispersed in 100 mL of a 20 mg/L TC solution and stirred magnetically for 30 min under dark conditions to establish adsorption–desorption equilibrium. A certain amount of H₂O₂ was added, while a 300 W Xe lamp ($\lambda \geq 420$ nm) was turned on at the same time, and about 3 mL of the suspension was taken out every 10 min, filtered through a 0.22 μ m filter tip to remove the catalyst, and the absorbance was measured at 357 nm by spectrophotometry to evaluate the efficiencies of the TC degradation by the different catalysts. Every run was measured 3 times, and the relative error was less than 5%.

3.4. TC Mineralization Experiment

The sampling procedure for TC mineralization was based on that of the catalytic experiment. A total organic carbon analyzer was used to monitor the filtrate, and the TOC removal efficiency of TC was calculated with the following equation:

$$\text{TOC removal efficiency} = \frac{\text{TOC}_0 - \text{TOC}_t}{\text{TOC}_0} \times 100\% \quad (9)$$

where TOC₀ is the initial TOC value of the TC solution, and TOC_t indicates the TOC value measured at any time *t*.

3.5. Trapping Test of Active Species

The active species in the degradation process were investigated using tert-butyl alcohol (TBA, 150 mM), p-benzoquinone (p-BQ, 10 mM), disodium ethylenediaminetetraacetate (EDTA-2Na, 10 mM), and furfuryl alcohol (FFA, 10 mM) to capture hydroxyl radicals ($\cdot\text{OH}$), superoxide radicals ($\cdot\text{O}_2^-$), photogenerated holes (h^+), and singlet oxygen ($^1\text{O}_2$), respectively, and the experimental procedure was consistent with that used for the photocatalytically assisted Fenton-like degradation of TC by 9%Co-CNK-OH.

4. Conclusions

In this study, Co-CNK-OH photocatalysts were prepared by a calcination–impregnation method, and the 9%Co-CNK-OH showed the best degradation efficiency (87.1% TC degradation in 40 min and 50% TOC removal in an hour). The doping of Co²⁺ expanded the absorption range of visible light and accelerated the transfer of the photogenerated electrons at the interface of the catalysts. The Co (III)/Co (II) redox cycle not only accelerated the consumption of the photogenerated electrons and then promoted the separation of the photogenerated electrons and holes but also accelerated the continuous generation of $^1\text{O}_2$, $\cdot\text{O}_2^-$, and h^+ in the system. The addition of H₂O₂ and the Co²⁺/Co³⁺ redox cycle pro-

moted the production of $^1\text{O}_2$ and $\cdot\text{O}_2^-$ and, thus, improved the TC degradation efficiency. The mechanism study of Co-CNK-OH for the Fenton-like photocatalytic degradation of TC was further proposed and confirmed that h^+ , $\cdot\text{O}_2^-$, and $^1\text{O}_2$ are the main reactive species in the TC degradation.

Supplementary Materials: The following supporting information can be downloaded at: <https://www.mdpi.com/article/10.3390/catal13040715/s1>, Figure S1: The influence of initial TC concentration(a), H_2O_2 concentration(b), pH value(c) and Catalyst addition (d) on degradation efficiency of TC.

Author Contributions: Conceptualization, J.W. and D.H.; methodology, D.H. and J.L.; experiments, D.H. and Q.S.; data curation, D.H., Q.S. and M.Z.; writing—original draft preparation, D.H.; guidance, review, and editing, J.W.; funding acquisition, J.W. All authors have read and agreed to the published version of the manuscript.

Funding: This research was funded by the National Natural Science Foundation of China (No. 22178326).

Data Availability Statement: The data generated during and/or analysed during the study are available from the corresponding author on reasonable request.

Conflicts of Interest: The authors declare that the research was conducted in the absence of any commercial or financial relationships that could be construed as potential conflicts of interest.

References

1. Zhou, Y.; Li, W.B.; Kumar, V.; Necibi, M.C.; Mu, Y.J.; Shi, C.Z.; Chaurasia, D.; Chauhan, S.; Chaturvedi, P.; Sillanpaa, M.; et al. Synthetic organic antibiotics residues as emerging contaminants waste-to-resources processing for a circular economy in China: Challenges and perspective. *Environ. Res.* **2022**, *211*, 113075. [[CrossRef](#)] [[PubMed](#)]
2. Li, C.; Tian, Q.; Zhang, Y.; Li, Y.; Yang, X.; Zheng, H.; Chen, L.; Li, F. Sequential combination of photocatalysis and microalgae technology for promoting the degradation and detoxification of typical antibiotics. *Water Res.* **2022**, *210*, 117985. [[CrossRef](#)] [[PubMed](#)]
3. Lu, Z.Y.; Huo, P.W.; Luo, Y.Y.; Liu, X.L.; Wu, D.; Gao, X.; Li, C.X.; Yan, Y.S. Performance of molecularly imprinted photocatalysts based on fly-ash cenospheres for selective photodegradation of single and ternary antibiotics solution. *J. Mol. Catal. A-Chem.* **2013**, *378*, 91–98. [[CrossRef](#)]
4. Sun, S.; Geng, J.; Ma, L.; Sun, X.; Qi, H.; Wu, Y.; Zhang, R. Changes in antibiotic resistance genotypes and phenotypes after two typical sewage disposal processes. *Chemosphere* **2022**, *291 Pt 2*, 132833. [[CrossRef](#)]
5. Conde-Cid, M.; Fernandez-Calvino, D.; Nunez-Delgado, A.; Fernandez-Sanjurjo, M.J.; Arias-Estevez, M.; Alvarez-Rodriguez, E. Estimation of adsorption/desorption Freundlich's affinity coefficients for oxytetracycline and chlortetracycline from soil properties: Experimental data and pedotransfer functions. *Ecotoxicol. Environ. Saf.* **2020**, *196*, 110584. [[CrossRef](#)] [[PubMed](#)]
6. Liu, P.X.; Zhang, H.M.; Feng, Y.J.; Yang, F.L.; Zhang, J.P. Removal of trace antibiotics from wastewater: A systematic study of nanofiltration combined with ozone-based advanced oxidation processes. *Chem. Eng. J.* **2014**, *240*, 211–220. [[CrossRef](#)]
7. Liu, M.; Xia, H.; Yang, W.; Liu, X.; Xiang, J.; Wang, X.; Hu, L.; Lu, F. Novel Cu-Fe bi-metal oxide quantum dots coupled g-C₃N₄ nanosheets with H₂O₂ adsorption-activation trade-off for efficient photo-Fenton catalysis. *Appl. Catal. B Environ.* **2022**, *301*, 120765. [[CrossRef](#)]
8. Bello, M.M.; Raman, A.A.A.; Asghar, A. A review on approaches for addressing the limitations of Fenton oxidation for recalcitrant wastewater treatment. *Process Saf. Environ. Prot.* **2019**, *126*, 119–140. [[CrossRef](#)]
9. Babuponnusami, A.; Muthukumar, K. Advanced oxidation of phenol: A comparison between Fenton, electro-Fenton, sono-electro-Fenton and photo-electro-Fenton processes. *Chem. Eng. J.* **2012**, *183*, 1–9. [[CrossRef](#)]
10. Qian, X.; Wu, Y.; Kan, M.; Fang, M.; Yue, D.; Zeng, J.; Zhao, Y. FeOOH quantum dots coupled g-C₃N₄ for visible light driving photo-Fenton degradation of organic pollutants. *Appl. Catal. B Environ.* **2018**, *237*, 513–520. [[CrossRef](#)]
11. Li, Y.; Luo, N.; Tian, Z.; Li, H.; Yang, M.; Shang, W.; Shen, Y.; Qu, M.; Zhou, A. H₂O₂-free photo-Fenton degradation of organic pollutants on thermally exfoliated g-C₃N₄. *Colloids Surf. A-Physicochem. Eng. Asp.* **2020**, *586*, 124190. [[CrossRef](#)]
12. Cui, K.P.; Yang, T.T.; Chen, Y.H.; Weerasooriya, R.; Li, G.H.; Zhou, K.; Chen, X. Magnetic recyclable heterogeneous catalyst Fe₃O₄/g-C₃N₄ for tetracycline hydrochloride degradation via photo-Fenton process under visible light. *Environ. Technol* **2022**, *43*, 3341–3354. [[CrossRef](#)]
13. Lu, N.; Liu, N.; Zhang, C.; Su, Y.; Shang, K.; Jiang, N.; Li, J.; Wu, Y. CO₂ conversion promoted by potassium intercalated g-C₃N₄ catalyst in DBD plasma system. *Chem. Eng. J.* **2021**, *417*, 129283. [[CrossRef](#)]
14. Lu, Z.-Z.; Li, S.-Q.; Xiao, J.-Y. Synergetic effect of Na-Ca for enhanced photocatalytic performance in NO_x degradation by g-C₃N₄. *Catal. Lett.* **2021**, *151*, 370–381. [[CrossRef](#)]

15. Zhou, M.; Jing, L.; Dong, M.; Lan, Y.; Xu, Y.; Wei, W.; Wang, D.; Xue, Z.; Jiang, D.; Xie, J. Novel broad-spectrum-driven g-C₃N₄ with oxygen-linked band and porous defect for photodegradation of bisphenol A, 2-mercaptophentiazole and ciprofloxacin. *Chemosphere* **2021**, *268*, 128839. [[CrossRef](#)]
16. Zhang, Q.; Peng, Y.; Deng, F.; Wang, M.; Chen, D. Porous Z-scheme MnO₂/Mn-modified alkalized g-C₃N₄ heterojunction with excellent Fenton-like photocatalytic activity for efficient degradation of pharmaceutical pollutants. *Sep. Purif. Technol.* **2020**, *246*, 116890. [[CrossRef](#)]
17. Lu, X.; Jin, Y.; Zhang, X.; Xu, G.; Wang, D.; Lv, J.; Zheng, Z.; Wu, Y. Controllable synthesis of graphitic C₃N₄/ultrathin MoS₂ nanosheet hybrid nanostructures with enhanced photocatalytic performance. *Dalton. Trans.* **2016**, *45*, 15406–15414. [[CrossRef](#)]
18. Thi Quyen, V.; Jae Kim, H.; Kim, J.; Thi Thu Ha, L.; Thi Huong, P.; My Thanh, D.; Minh Viet, N.; Quang Thang, P. Synthesizing S-doped graphitic carbon nitride for improvement photodegradation of tetracycline under solar light. *Sol. Energy* **2021**, *214*, 288–293. [[CrossRef](#)]
19. Bao, J.; Bai, W.; Wu, M.; Gong, W.; Yu, Y.; Zheng, K.; Liu, L. Template-mediated copper doped porous g-C₃N₄ for efficient photodegradation of antibiotic contaminants. *Chemosphere* **2022**, *293*, 133607. [[CrossRef](#)]
20. Zhou, M.; Dong, G.; Yu, F.; Huang, Y. The deep oxidation of NO was realized by Sr multi-site doped g-C₃N₄ via photocatalytic method. *Appl. Catal. B Environ.* **2019**, *256*, 117825. [[CrossRef](#)]
21. Wu, X.; Chen, F.; Wang, X.; Yu, H. In situ one-step hydrothermal synthesis of oxygen-containing groups-modified g-C₃N₄ for the improved photocatalytic H₂-evolution performance. *Appl. Surf. Sci.* **2018**, *427*, 645–653. [[CrossRef](#)]
22. Shi, Y.X.; Li, L.L.; Xu, Z.; Sun, H.R.; Guo, F.; Shi, W.L. One-step simple green method to prepare carbon-doped graphitic carbon nitride nanosheets for boosting visible-light photocatalytic degradation of tetracycline. *J. Chem. Technol. Biotechnol.* **2021**, *96*, 3122–3133. [[CrossRef](#)]
23. Wu, X.; Gao, D.; Wang, P.; Yu, H.; Yu, J. NH₄Cl-induced low-temperature formation of nitrogen-rich g-C₃N₄ nanosheets with improved photocatalytic hydrogen evolution. *Carbon* **2019**, *153*, 757–766. [[CrossRef](#)]
24. Hu, C.; Liu, Z.-T.; Andrew Lin, K.-Y.; Wei, W.-H.; Wang, K.-H. Synergistic effect of KCl mixing and melamine/urea mixture in the synthesis of g-C₃N₄ for photocatalytic removal of tetracycline. *J. Ind. Eng. Chem.* **2022**, *107*, 118–125. [[CrossRef](#)]
25. Song, H.; Liu, L.; Wang, H.; Feng, B.; Xiao, M.; Tang, Y.; Qu, X.; Gai, H.; Huang, T. Adjustment of the band gap of Co-doped KCl/NH₄Cl/g-C₃N₄ for enhanced photocatalytic performance under visible light. *Mater. Sci. Semicond. Process.* **2021**, *128*, 105757. [[CrossRef](#)]
26. Cong, Y.; Chen, X.; Zheng, Q.; Zhang, Y.; Lv, S.W. The calcium alginate-immobilized Co-g-C₃N₄ composite microspheres as an efficient mediator to activate peroxydisulfate for degrading organic pollutants. *Environ. Res* **2022**, *215 Pt 2*, 114414. [[CrossRef](#)] [[PubMed](#)]
27. Wang, X.L.; Fang, W.Q.; Wang, H.F.; Zhang, H.; Zhao, H.; Yao, Y.; Yang, H.G. Surface hydrogen bonding can enhance photocatalytic H₂ evolution efficiency. *J. Mater. Chem. A* **2013**, *1*, 14089–14096. [[CrossRef](#)]
28. Li, Y.; Ouyang, S.; Xu, H.; Wang, X.; Bi, Y.; Zhang, Y.; Ye, J. Constructing Solid-Gas-Interfacial Fenton Reaction over Alkalized-C₃N₄ Photocatalyst to Achieve Apparent Quantum Yield of 49% at 420 nm. *J. Am. Chem. Soc.* **2016**, *138*, 13289–13297. [[CrossRef](#)] [[PubMed](#)]
29. Muhammad Azam, Q.; Mohsin, J.; Sammia, S.; Mudassar, S. Fabrication of g-C₃N₄/transition metal (Fe, Co, Ni, Mn and Cr)-doped ZnO ternary composites: Excellent visible light active photocatalysts for the degradation of organic pollutants from wastewater. *Mater. Res. Bull.* **2021**, *147*, 111630.
30. Chen, P.-W.; Li, K.; Yu, Y.-X.; Zhang, W.-D. Cobalt-doped graphitic carbon nitride photocatalysts with high activity for hydrogen evolution. *Appl. Surf. Sci.* **2017**, *392*, 608–615. [[CrossRef](#)]
31. Dong, Q.; Chen, Y.; Wang, L.; Ai, S.; Ding, H. Cu-modified alkalized g-C₃N₄ as photocatalytically assisted heterogeneous Fenton-like catalyst. *Appl. Surf. Sci.* **2017**, *426*, 1133–1140. [[CrossRef](#)]
32. Wu, Y.; Zhao, X.; Huang, S.; Li, Y.; Zhang, X.; Zeng, G.; Niu, L.; Ling, Y.; Zhang, Y. Facile construction of 2D g-C₃N₄ supported nanoflower-like NaBiO₃ with direct Z-scheme heterojunctions and insight into its photocatalytic degradation of tetracycline. *J. Hazard. Mater.* **2021**, *414*, 125547. [[CrossRef](#)] [[PubMed](#)]
33. Nie, H.; Ou, M.; Zhong, Q.; Zhang, S.; Yu, L. Efficient visible-light photocatalytic oxidation of gaseous NO with graphitic carbon nitride (g-C₃N₄) activated by the alkaline hydrothermal treatment and mechanism analysis. *J. Hazard. Mater.* **2015**, *300*, 598–606. [[CrossRef](#)]
34. Gao, Y.H.; Zhao, W.L.; Chen, Y. g-C₃N₄ modified by hydroxyl group on the surface prepared by double salt enhanced the visible light photocatalytic activity. *Diam. Relat. Mater.* **2021**, *116*, 108425. [[CrossRef](#)]
35. Tang, Q.; Sun, Z.; Deng, S.; Wang, H.; Wu, Z. Decorating g-C₃N₄ with alkalized Ti₃C₂ Mxene for promoted photocatalytic CO₂ reduction performance. *J. Colloid. Interface Sci.* **2020**, *564*, 406–417. [[CrossRef](#)]
36. Papailias, I.; Todorova, N.; Giannakopoulou, T.; Ioannidis, N.; Boukos, N.; Athanasekou, C.P.; Dimotikali, D.; Trapalis, C. Chemical vs thermal exfoliation of g-C₃N₄ for NO_x removal under visible light irradiation. *Appl. Catal. B Environ.* **2018**, *239*, 16–26. [[CrossRef](#)]
37. Li, Z.; Wu, Y.; Lu, G. Highly Efficient Hydrogen Evolution over Co(OH)₂ Nanoparticles Modified g-C₃N₄ Co-sensitized by Eosin Y and Rose Bengal under Visible Light Irradiation. *Appl. Catal. B Environ.* **2016**, *188*, 56–64. [[CrossRef](#)]
38. Liu, Q.; Zhang, J. Graphene supported Co-g-C₃N₄ as a novel metal-macrocylic electrocatalyst for the oxygen reduction reaction in fuel cells. *Langmuir* **2013**, *29*, 3821–3828. [[CrossRef](#)] [[PubMed](#)]

39. Zhao, N.; Kong, L.; Dong, Y.; Wang, G.; Wu, X.; Jiang, P. Insight into the crucial factors for photochemical deposition of cobalt cocatalysts on g-C₃N₄ Photocatalysts. *ACS Appl. Mater. Interfaces* **2018**, *10*, 9522–9531. [[CrossRef](#)]
40. Li, J.; Chen, C.; Qin, F.; Jiang, Y.; An, H.; Fang, J.; Zhang, K.; Lai, Y. Mesoporous Co–N–C composite as a sulfur host for high-capacity and long-life lithium–sulfur batteries. *J. Mater. Sci.* **2018**, *53*, 13143–13155. [[CrossRef](#)]
41. Yu, J.; Chen, G.; Sunarso, J.; Zhu, Y.; Ran, R.; Zhu, Z.; Zhou, W.; Shao, Z. Cobalt oxide and cobalt-graphitic carbon core-shell based catalysts with remarkably high oxygen reduction reaction activity. *Adv. Sci.* **2016**, *3*, 1600060. [[CrossRef](#)]
42. Zhang, C.; Qin, D.; Zhou, Y.; Qin, F.; Wang, H.; Wang, W.; Yang, Y.; Zeng, G. Dual optimization approach to Mo single atom dispersed g-C₃N₄ photocatalyst: Morphology and defect evolution. *Appl. Catal. B Environ.* **2022**, *303*, 120904. [[CrossRef](#)]
43. Shi, Y.; Zhao, Q.; Li, J.; Gao, G.; Zhi, J. Onion-like carbon-embedded graphitic carbon nitride for enhanced photocatalytic hydrogen evolution and dye degradation. *Appl. Catal. B: Environ.* **2022**, *308*, 121216. [[CrossRef](#)]
44. Chen, T.; Yin, D.; Zhao, F.; Kyu, K.K.; Liu, B.; Chen, D.; Huang, K.; Deng, L.; Li, L. Fabrication of 2D heterojunction photocatalyst Co-g-C₃N₄/MoS₂ with enhanced solar-light-driven photocatalytic activity. *New J. Chem.* **2019**, *43*, 463–473. [[CrossRef](#)]
45. Wang, Z.; Wang, H.; Wang, Z.; Huang, D.; Qin, H.; He, Y.; Chen, M.; Zeng, G.; Xu, P. Ferrocene modified g-C₃N₄ as a heterogeneous catalyst for photo-assisted activation of persulfate for the degradation of tetracycline. *Colloids Surf. A Physicochem. Eng. Asp.* **2021**, *626*, 127024. [[CrossRef](#)]
46. Yang, G.; Liang, Y.J.; Xiong, Z.R.; Yang, J.; Wang, K.; Zeng, Z.K. Molten salt-assisted synthesis of Ce₄O₇/Bi₄MoO₉ heterojunction photocatalysts for photo-Fenton degradation of tetracycline: Enhanced mechanism, degradation pathway and products toxicity assessment. *Chem. Eng. J.* **2021**, *425*, 130689. [[CrossRef](#)]
47. Shi, C.D.; Yu, S.Y.; Li, C.J. Fabrication of aligned carbon nanofiber doped with SnO₂-Sb for efficient electrochemical removal of tetracycline. *Chem. Eng. J.* **2022**, *441*, 136052. [[CrossRef](#)]
48. Duan, R.; Ma, S.; Xu, S.; Wang, B.; He, M.; Li, G.; Fu, H.; Zhao, P. Soybean straw biochar activating peroxydisulfate to simultaneously eliminate tetracycline and tetracycline resistance bacteria: Insights on the mechanism. *Water Res.* **2022**, *218*, 118489. [[CrossRef](#)]
49. Sun, H.; Wang, L.; Guo, F.; Shi, Y.; Li, L.; Xu, Z.; Yan, X.; Shi, W. Fe-doped g-C₃N₄ derived from biowaste material with Fe-N bonds for enhanced synergistic effect between photocatalysis and fenton degradation activity in a broad pH range. *J. Alloy. Compd.* **2022**, *900*, 163410. [[CrossRef](#)]
50. Bai, X.; Wang, X.; Lu, X.; Liang, Y.; Li, J.; Wu, L.; Li, H.; Hao, Q.; Ni, B.-J.; Wang, C. Surface defective g-C₃N_{4-x}Cl_x with unique spongy structure by polarization effect for enhanced photocatalytic removal of organic pollutants. *J. Hazard. Mater.* **2020**, *398*, 122897. [[CrossRef](#)]
51. Liu, X.; Li, Y.; Fan, X.; Zhang, F.; Zhang, G.; Peng, W. Photo-accelerated Co³⁺/Co²⁺ transformation on cobalt and phosphorus Co-doped g-C₃N₄ for Fenton-like reaction. *J. Mater. Chem. A* **2021**, *9*, 22399–22409. [[CrossRef](#)]

Disclaimer/Publisher's Note: The statements, opinions and data contained in all publications are solely those of the individual author(s) and contributor(s) and not of MDPI and/or the editor(s). MDPI and/or the editor(s) disclaim responsibility for any injury to people or property resulting from any ideas, methods, instructions or products referred to in the content.